

[C II] 158 μ m Emission from the Host Galaxies of Damped Lyman Alpha Systems

Marcel Neeleman^{1*}, Nissim Kanekar², J. Xavier Prochaska¹, Marc Rafelski³,
Chris L. Carilli^{4,5}, Arthur M. Wolfe^{6†}

¹University of California Observatories-Lick Observatory,
University of California, Santa Cruz, CA, 95064, USA

²National Centre for Radio Astrophysics, Tata Institute of Fundamental Research,
Pune University, Pune 411007, India

³Space Telescope Science Institute, Baltimore, MD 21218, USA

⁴National Radio Astronomy Observatory, Socorro, NM 87801, USA

⁵Cavendish Laboratory, University of Cambridge,
19 J. J. Thomson Ave., Cambridge CB3 0HE, UK

⁶Department of Physics and Center for Astrophysics and Space Sciences,
University of California, San Diego, CA, 95064, USA

[†]Deceased

*Corresponding author. E-mail: marcel@ucsc.edu.

Gas surrounding high redshift galaxies has been studied through observations of absorption line systems toward background quasars for decades. However, it has proven difficult to identify and characterize the galaxies associated with these absorbers due to the intrinsic faintness of the galaxies compared to the quasars at optical wavelengths. Utilizing the Atacama Large Millimeter/Submillimeter Array, we report on detections of [C II] 158 μ m line and dust continuum emission from two galaxies associated with two such absorbers at a redshift of $z \sim 4$. Our results indicate that the hosts of these high-metallicity

absorbers have physical properties similar to massive star-forming galaxies and are embedded in enriched neutral hydrogen gas reservoirs that extend well beyond the star-forming interstellar medium of these galaxies.

Gas plays a crucial role in the formation of galaxies by providing the fuel for star formation. However, the initial overdensities of baryons and dark matter from which galaxies form do not contain enough gas to sustain the observed star formation rate (SFR) of galaxies (1, 2). Galaxies must therefore accrete gas from their surroundings. A comprehensive understanding of the accreting gas, in particular neutral hydrogen (H I) gas, which is a crucial component (2), is thus critical for understanding the formation and evolution of galaxies. Unfortunately, observing H I gas in emission from galaxies at cosmological distances is challenging because of the intrinsic weakness of its most reliable tracer, the H I 21 cm hyperfine structure line. This line is difficult to detect at even moderate redshifts with today's telescopes (3), and at high redshifts, $z \geq 1$, we must rely on studying H I gas in absorption.

As light from a bright background source, such as a quasar, travels toward us, it encounters pockets of H I gas which imprint a characteristic absorption signature in the spectrum due to absorption at the frequency of the redshifted Lyman-alpha (Ly- α) line. The strongest H I absorption features in quasar spectra have H I column densities $\geq 2 \times 10^{20} \text{ cm}^{-2}$, and are known as damped Ly- α Absorbers (DLAs) because their Ly- α absorption line profiles show distinctive damping wings (4). Observations of DLAs have revealed a wealth of information on the properties of the absorbing gas, including its kinematical signatures (5), metal enrichment (6), dust content (7) and temperature (8). Moreover, DLAs have been intimately linked to galaxies through direct imaging studies at intermediate redshifts (9, 10), scaling relations (11, 12), and cosmological simulations (13, 14). Surveys of DLAs therefore provide a powerful means to study H I gas surrounding high redshift galaxies.

Unfortunately, directly detecting the starlight from the foreground galaxy that is associated

with the DLA is challenging at optical wavelengths, owing to the presence of the much brighter background quasar (15). As a result, despite many recent searches (10, 16–18), there are only a handful of high-redshift DLAs whose host galaxies have been identified by imaging studies. As such, there is little direct observational data on the nature of the galaxies that give rise to DLAs at different redshifts, including their mass, SFR, and the extent of the neutral H I gas surrounding the galaxy. At the same time, extensive data is available from deep optical and near-infrared surveys on the stellar properties of luminosity-selected galaxies (19–21), but little is known about the gas surrounding these galaxies. A crucial link is therefore missing in connecting high redshift galaxies with the gaseous envelopes that shape their evolution.

We report here on a search for the galaxies associated with two DLAs at $z \sim 4$ using the Atacama Large Millimeter/Sub-millimeter Array (ALMA). At sub-millimeter wavelengths, the background quasars emit little radiation, enabling a search for the host galaxy of the DLA at close angular separation (impact parameter) from the quasar. The DLAs towards quasars SDSS J081740.52+135134.5 and SDSS J120110.31+211758.5 were selected from a large sample of DLAs because of their higher than average metal content (6). We used ALMA to carry out a search for emission in both the singly-ionized carbon fine-structure line at a rest wavelength of $157.74 \mu\text{m}$ ([C II] $158\mu\text{m}$) and the far-infrared (FIR) dust continuum from the two DLA host galaxies (22). The [C II] $158\mu\text{m}$ line is expected to be the strongest FIR line from galaxies at these redshifts (23), in part because it is the primary coolant of cold H I gas (24), and because it is the strongest observed FIR line in the local Universe (25).

In each of the ALMA observations, we detect a $>6\sigma$ emission feature at the frequency of the redshifted [C II] $158\mu\text{m}$ line at $z = 4.2601$ and $z = 3.7978$, which is offset from the quasar position by $6.2''$ and $2.5''$, for SDSS J081740.52+135134.5 and SDSS J120110.31+211758.5, respectively (Fig. 1). The redshifts of the DLAs, as measured from low ionization atomic absorption lines (e.g., singly ionized iron and silicon), and the [C II] $158\mu\text{m}$ emission (Fig. 2)

are within 100 km s^{-1} of each other (Fig. 2). The close proximity in both redshift space and angular separation on the sky indicates that the [C II] $158\mu\text{m}$ emission must come from a galaxy associated with the DLA.

Our [C II] $158\mu\text{m}$ images are sensitive to the kinematics of the galaxy, as any gas motion will yield a Doppler shift in the observed [C II] $158\mu\text{m}$ line frequency. Since the emission is only barely resolved spatially, the kinematic signature of the gas is best described by a position-velocity (p - v) diagram (Fig. 3). For ALMA J081740.86+135138.2, the shape of the emission is indicative of rotation, which is corroborated by the ‘double-horned’ profile seen in the [C II] $158\mu\text{m}$ emission spectrum (Fig. 2). From the magnitude of the rotation, we estimate a lower limit to the dynamical mass of 6×10^{10} solar masses (M_{\odot}) for this galaxy (22). For ALMA J120110.26+211756.2, the p - v diagram suggests more complicated gas dynamics which is corroborated by the spatial offset between the redshifted and blueshifted components (22).

FIR dust continuum emission co-spatial with the [C II] $158\mu\text{m}$ emission is also detected in the ALMA observations (Fig 1). The dust continuum yields estimates of the SFR, as emission is due to reprocessed starlight, mainly from the youngest stars (22). We find that both galaxies are forming stars at moderately high rates, with SFR of $110 \pm 10 M_{\odot} \text{ yr}^{-1}$ for ALMA J081740.86+135138.2 and $24 \pm 8 M_{\odot} \text{ yr}^{-1}$ for ALMA J120110.26+211756.2. The total far-infrared (TIR) luminosities of the galaxies are estimated by fitting a modified black body spectrum to the observed FIR dust continuum measurement. The properties of the galaxies are tabulated in Table S2.

The observations enable a comparison between the properties of these absorption-selected galaxies and the properties of emission-selected galaxies observed at similar redshifts, such as Lyman-break galaxies (LBGs). LBGs are star-forming galaxies identified in photometric studies by their characteristic rest-frame ultraviolet luminosity deficit. This deficit is due to the absorption of photons blueward of the Lyman continuum break (26). The observed SFRs of the two absorption-selected galaxies are comparable to the SFR of bright LBGs at similar

redshift (27). However, by selecting the DLAs on their high metallicity, we are probing the massive end of the distribution of DLA host galaxies (11, 12). The typical galaxies associated with DLAs likely have a smaller mass, and thus, a smaller SFR, consistent with non-detections reported in the literature (17).

Plotting the [C II] 158 μ m line luminosity versus the SFR for high-redshift ($z \geq 1$) galaxies (Fig. 4a) shows that our absorption-selected galaxies occupy the same parameter space as high-redshift, emission-selected galaxies, and fall within one standard deviation of the correlation found in the local Universe between these two observables (28). Similarly, the two absorption-selected galaxies fall within the same parameter space as their high-redshift emission-selected counterparts in a plot of the ratio of [C II] 158 μ m line luminosity to TIR luminosity versus TIR luminosity (Fig. 4b). This strengthens the assertion that high-metallicity, absorption-selected galaxies are similar to moderately star-forming, emission-selected galaxies, such as the massive end of the LBG population. This assertion is further corroborated by the agreement between our dynamical mass estimate in ALMA J081740.86+135138.2 and the dynamical mass estimates of comparable emission-selected galaxies at $z \sim 5$ (27). The observed connection between massive LBGs and high-metallicity DLAs supports results from earlier DLA studies at lower redshifts (9, 29) and cross-correlation studies with the Ly α forest (30).

We can use the impact parameter estimates to probe the physical extent of the H I gas around absorption-selected galaxies. The observed impact parameters correspond to physical (proper) distances of 42 kpc and 18 kpc at the DLA redshifts for ALMA J081740.86+135138.2 and ALMA J120110.26+211756.2, respectively. These distances are substantially larger than the extent of the [C II] 158 μ m line emission, which extends to ~ 5 kpc, and indicate that these galaxies have large reservoirs of H I relatively far away from their star-forming regions. The observed distances also require that the emission and absorption lines arise in physically separated gas. Therefore, the absorbing gas must probe either H I gas associated with a satellite

galaxy, an enriched neutral outflow from the galaxy, or H I gas in the inner circumgalactic medium/extended disk of the galaxy. The first explanation is disfavored, because the satellite galaxies would need to be metal-enriched and show highly turbulent velocity dispersions of several hundreds of km s^{-1} , indicative of massive star-forming systems. However, little star-formation is observed, as no [C II] $158\mu\text{m}$ emission is seen at the position of the absorber.

The absorbing gas is therefore more likely to reside in the inner gaseous halo of each DLA host galaxy. For the DLA towards SDSS J081740.52+135134.5, the gas is systematically blueshifted along the same direction and with the same magnitude as the rotation of the cool gas disk observed in [C II] $158\mu\text{m}$ line emission. This could indicate that the gas detected in absorption is co-rotating in an extended disk. Most simulations predict precisely such an extended planar configuration fed by cold flows (31) with properties similar to those observed in the $z = 4.26$ DLA (32). The DLA towards SDSS J120110.31+211758.5 is harder to classify because its absorption is seen over the full velocity range of the emission profile, which spans almost 500 km s^{-1} . This is more indicative of a large-scale outflow or a highly perturbed system, which is corroborated by the spatial shift in the [C II] $158\mu\text{m}$ line emission (Fig. S2). In both cases, it is clear that the DLA host galaxy has effectively enriched its inner gaseous halo, in agreement with recent simulations (33).

Our results indicate that the galaxies giving rise to high-metallicity DLAs have characteristics similar to the high mass end of the LBG population (9, 30), and are embedded in a large reservoir of neutral H I gas. This gas is being enriched by the galaxy, but is bound to it, as there is almost no systematic velocity offset between the metals seen in absorption and the [C II] $158\mu\text{m}$ line in emission. This suggests that this halo gas will eventually accrete back onto the galaxy providing enriched gas for future star formation.

References and Notes

1. J. X. Prochaska, S. Herbert-Fort, A. M. Wolfe, *Astrophys. J.* **635**, 123 (2005).
2. D. Kereš, N. Katz, D. H. Weinberg, R. Davé, *Mon. Not. R. Astron. Soc.* **363**, 2 (2005).
3. X. Fernández, *et al.*, *Astrophys. J.* **824**, L1 (2016).
4. A. Wolfe, E. Gawiser, J. Prochaska, *Annu. Rev. Astron. Astrophys.* **43**, 861 (2005).
5. J. Prochaska, A. Wolfe, *Astrophys. J.* **487**, 73 (1997).
6. M. Rafelski, A. Wolfe, J. Prochaska, M. Neeleman, A. Mendez, *Astrophys. J.* **755**, 89 (2012).
7. M. Pettini, L. Smith, R. Hunstead, D. King, *Astrophys. J.* **426**, 79 (1994).
8. N. Kanekar, *et al.*, *Mon. Not. R. Astron. Soc.* **438**, 2131 (2014).
9. P. Møller, S. Warren, S. M. Fall, J. Fynbo, P. Jakobsen, *Astrophys. J.* **574**, 51 (2002).
10. J.-K. Krogager, *et al.*, *Mon. Not. R. Astron. Soc.* **424**, 1 (2012).
11. M. Neeleman, A. Wolfe, J. Prochaska, M. Rafelski, *Astrophys. J.* **769**, 54 (2013).
12. L. Christensen, P. Møller, J. Fynbo, T. Zafar, *Mon. Not. R. Astron. Soc.* **445**, 225 (2014).
13. R. Cen, *Astrophys. J.* **748**, 121 (2012).
14. S. Bird, *et al.*, *Mon. Not. R. Astron. Soc.* **445**, 2313 (2014).
15. J. P. U. Fynbo, *et al.*, *Mon. Not. R. Astron. Soc.* **408**, 2128 (2010).
16. C. Péroux, N. Bouché, V. Kulkarni, D. York, G. Vladilo, *Mon. Not. R. Astron. Soc.* **410**, 2237 (2011).

17. M. Fumagalli, J. O’Meara, J. Prochaska, M. Rafelski, N. Kanekar, *Mon. Not. R. Astron. Soc.* **446**, 3178 (2015).
18. R. Srianand, *et al.*, *Mon. Not. R. Astron. Soc.* **460**, 634 (2016).
19. M. Giavalisco, *et al.*, *Astrophys. J.* **600**, 93 (2004).
20. S. V. W. Beckwith, *et al.*, *Astron. J.* **132**, 1729 (2006).
21. N. A. Grogin, *et al.*, *Astrophys. J. Suppl. Ser.* **197**, 35 (2011).
22. Materials and methods are available as supplementary materials on *Science Online*.
23. C. Carilli, F. Walter, *Annu. Rev. Astron. Astrophys.* **51**, 105 (2013).
24. J. Pineda, W. Langer, T. Velusamy, P. Goldsmith, *Astron. Astrophys.* **554**, 103 (2013).
25. S. Malhotra, *et al.*, *Astrophys. J.* **561**, 766 (2001).
26. C. C. Steidel, M. Giavalisco, M. Dickinson, K. L. Adelberger, *Astron. J.* **112**, 352 (1996).
27. P. L. Capak, *et al.*, *Nature* **522**, 455 (2015).
28. I. De Looze, *et al.*, *Astron. Astrophys.* **568**, 62 (2014).
29. M. Rafelski, *et al.*, *Astrophys. J.* **825**, 87 (2016).
30. A. Font-Ribera, *et al.*, *J. Cosm. Astropart. Phys.* **11**, 59 (2012).
31. K. R. Stewart, *et al.*, *Astrophys. J.* **769**, 74 (2013).
32. M. Danovich, A. Dekel, O. Hahn, D. Ceverino, J. Primack, *Mon. Not. R. Astron. Soc.* **449**, 2087 (2015).
33. A. L. Muratov, *et al.*, *Mon. Not. R. Astron. Soc.* **454**, 2691 (2015).

34. ALMA Partnership, *et al.*, “ALMA Cycle 4 Technical Handbook” (2016; <https://almascience.nrao.edu/documents-and-tools/cycle4/alma-technical-handbook>).
35. J. P. McMullin, B. Waters, D. Schiebel, W. Young, K. Golap, *Astronomical Data Analysis Software and Systems XVI*, R. A. Shaw, F. Hill, D. J. Bell, eds. (2007), vol. 376, p. 127.
36. E. W. Greisen, *Information Handling in Astronomy - Historical Vistas* **285**, 109 (2003).
37. S. S. Vogt, *et al.*, *Instrumentation in Astronomy VIII*, Crawford, D. L. and Craine, E. R., ed. (1994), vol. 2198 of *Proc. SPIE*, p. 362.
38. M. Asplund, N. Grevesse, A. J. Sauval, P. Scott, *Annu. Rev. Astron. Astrophys.* **47**, 481 (2009).
39. P. M. Solomon, D. Downes, S. J. E. Radford, J. W. Barrett, *Astrophys. J.* **478**, 144 (1997).
40. P. F. Goldsmith, W. D. Langer, J. L. Pineda, T. Velusamy, *Astrophys. J. Suppl. Ser.* **203**, 13 (2012).
41. D. Calzetti, *et al.*, *Astrophys. J.* **714**, 1256 (2010).
42. C. Lonsdale Persson, G. Helou, *Astrophys. J.* **314**, 513 (1987).
43. R. Wang, *et al.*, *Astrophys. J.* **773**, 44 (2013).
44. M. Neeleman, *et al.*, *Astrophys. J.* **820**, L39 (2016).
45. K. N. Abazajian, *et al.*, *Astrophys. J. Suppl. Ser.* **182**, 543 (2009).
46. Support for this work was provided by the NSF through award SOSPA2-002 from the NRAO. MN and JXP are partially supported by a grant from the National Science Foundation (AST-1412981). NK acknowledges support from the Department of Science and

Technology via a Swarnajayanti Fellowship (DST/SJF/PSA-01/2012-13), and MR was partially supported by a NASA Postdoctoral Program fellowship. ALMA is a partnership of ESO (representing its member states), NSF (USA) and NINS (Japan), together with NRC (Canada), NSC and ASIAA (Taiwan), and KASI (Republic of Korea), in cooperation with the Republic of Chile. The Joint ALMA Observatory is operated by ESO, AUI/NRAO and NAOJ. Part of the data presented herein were obtained at the W.M. Keck Observatory, which is operated as a scientific partnership among the California Institute of Technology, the University of California and the National Aeronautics and Space Administration. The Observatory was made possible by the generous financial support of the W.M. Keck Foundation. The authors wish to recognize and acknowledge the very significant cultural role and reverence that the summit of Mauna Kea has always had within the indigenous Hawaiian community. We are most fortunate to have the opportunity to conduct observations from this mountain. Finally we wish to acknowledge the Esalen Institute, whose natural beauty was the catalyst for writing this paper. The data reported in this paper are available through the ALMA archive (<https://almascience.nrao.edu/alma-data/archive>) with project code: ADS/JAO.ALMA#2015.1.01564.S, and the Keck Observatory Archive (<https://koa.ipac.caltech.edu>) with program ID: U163HR.

Supporting Material

Supporting text

Figures S1 -S2

Tables S1 - S4

References (34–45)

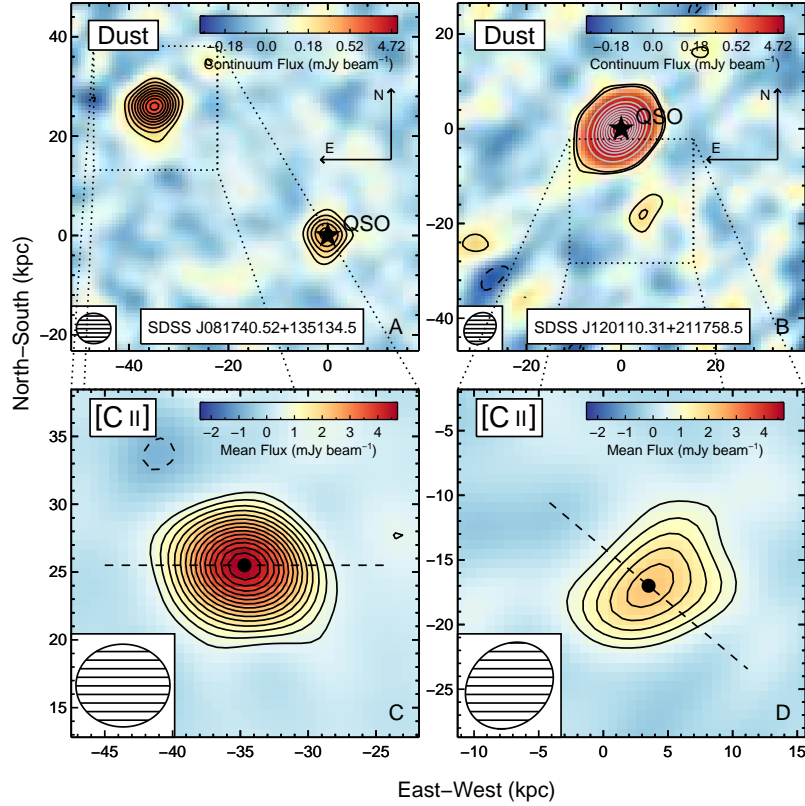


Fig. 1. 400 GHz continuum and [C II] 158 μ m emission from two DLA fields. Panels A and B show the ≈ 400 GHz continuum emission from the regions surrounding two quasars (black stars). Black contours begin at 3σ and increase by $\sqrt{2}\sigma$; dashed contours indicate negative values. Gray contours are drawn at increments of 25σ . The axes give the relative physical (proper) distance at the DLA redshifts (i.e., $z = 4.2584$ and $z = 3.7975$ for SDSS J081740.52+135134.5 and SDSS J120110.31+211758.5, respectively). Panels C and D show the mean flux density over the full [C II] 158 μ m line profile displayed in panels A and B of Fig. 2 for a smaller region centered on the identified DLA host galaxies. No other emission lines are detected in these fields. The line contours begin at 3σ , with each subsequent contour increasing by $\sqrt{2}\sigma$. The size of the synthesized beam is shown in the bottom left of each panel. The dashed line is the measured major axis of the galaxy QSO, quasar or quasi-stellar object (22).

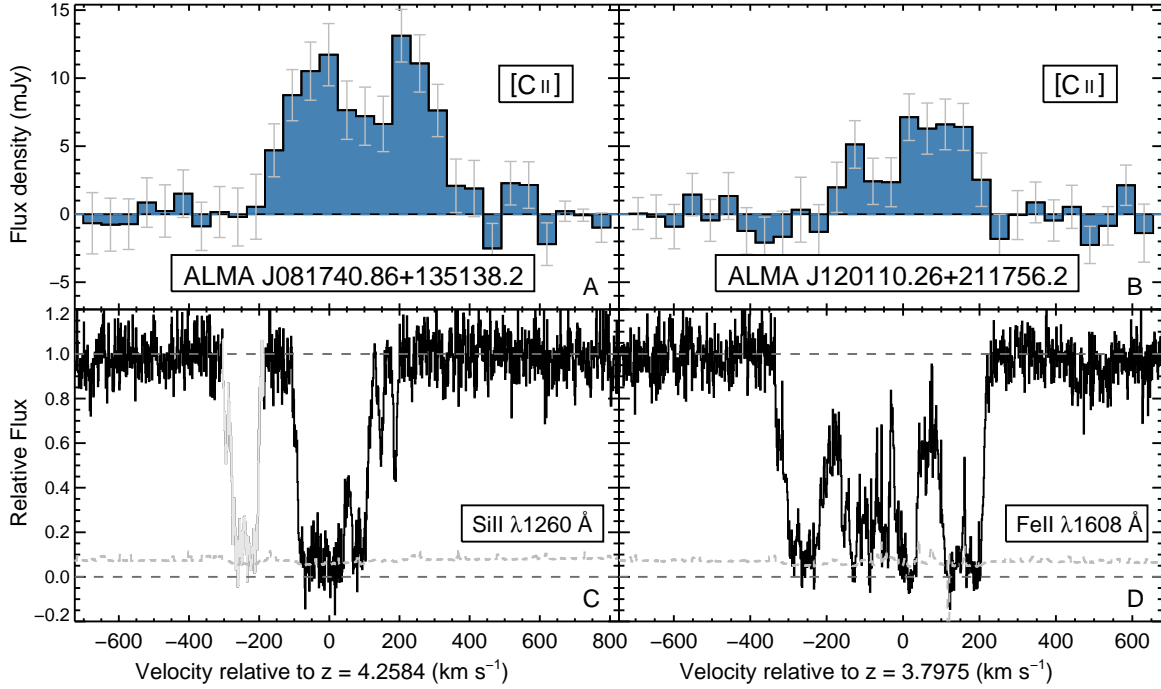


Fig. 2. Emission and absorption spectra from the host galaxies and DLAs. Panels A and B show the [C II] 158 μ m emission profile for the galaxy hosts identified with two high redshift DLAs (Fig. 1). The 1σ uncertainties are shown in gray. The zero-point of the velocity scale was chosen to correspond with the strongest absorption feature of the DLAs (panels C and D). The absorption profiles are for two representative low-ionization elements, singly ionized silicon and singly ionized iron, which trace the bulk of the metals in the absorbers. The grayed-out region in panel C is a sulfur absorption line (S II λ 1259 \AA). The agreement in redshift and width of the absorption and emission lines indicate that the [C II] 158 μ m emission is from the DLA host galaxy.

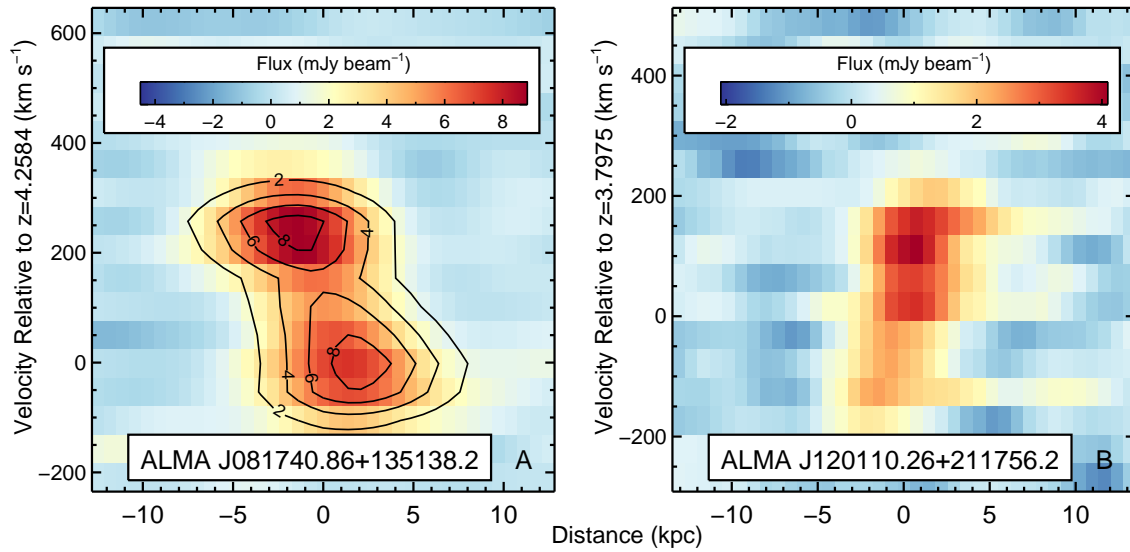


Fig. 3. Position-velocity ($dv-v$) diagrams for the [C II] 158 μm emission. The distance is calculated from the center of the [C II] 158 μm emission along the observed major axis of the galaxy (Fig. 1). For ALMA J081740.86+135138.2, a model of a simple uniformly-rotating disk is shown in contours (22). The agreement between this model and the data suggest that the [C II] 158 μm line originates from a cool gaseous disk. For ALMA J120110.26+211756.2, the [C II] 158 μm emission appears more complicated, albeit at a lower signal-to-noise ratio. mJy, milijansky.

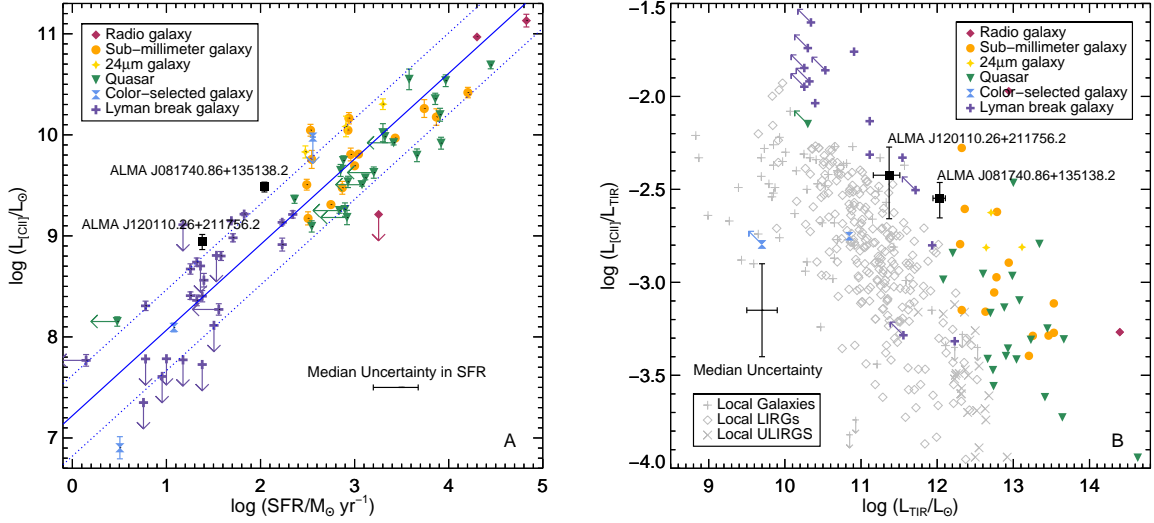


Fig. 4. Comparison of observed properties of the DLA hosts with local and high redshift galaxies. Panel A shows the correlation between the [C II] 158μm luminosity and star formation rate (SFR) for a sample of $z > 1$ galaxies categorized by galaxy type (23). Also plotted is the correlation for galaxies in the local Universe (blue line), along with the associated scatter (blue dashed lines) (28). Panel B shows the ratio of [C II] 158μm luminosity to total infrared (TIR) luminosity, L_{TIR} as a function of L_{TIR} for the same sample of $z > 1$ galaxies. Plotted in gray are a sample of local galaxies and local (ultra) luminous infrared galaxies, (U)LIRGs. The high-metallicity, absorption-selected galaxies occupy the same parameter space as moderately star-forming, emission-selected galaxies at similar redshift, suggesting that they have similar characteristics. L_{\odot} , luminosity of the Sun. Error bars indicate 1σ .

Materials and Methods

Cosmology

Throughout this paper we use a flat Λ cold dark matter cosmology, defined by the parameters, $\Omega_\Lambda = 0.7$, $\Omega_M = 0.3$ and $H_0 = 70 \text{ km s}^{-1}$. Adopting this cosmology facilitates comparison with previous results in the literature.

Observations, Data Reduction and Analysis

ALMA (34) observed the two fields surrounding quasars SDSS J081740.52+135134.5 and SDSS J120110.31+211758.5 over a span of four days from 2015 December 29 to 2016 January 1 (all dates are given in Universal Time). Total on-source integration times on the two quasar fields were 46 minutes and 76 minutes, respectively. One of the ALMA 1.875 GHz bands was centered on the expected redshifted frequency of the [C II] 158 μm line, with the expected [C II] 158 μm redshift determined from the strongest metal line absorption feature seen in the QSO absorption spectrum (Fig. 3). The remaining three 2 GHz bands were set to measure the continuum emission in the quasar fields. Exact details of the instrument configuration are given in Table S1. A third quasar, SDSS J144331.17+272436.7, was also observed in May 2016 as part of the same program. However, problems with quality assurance meant that the data for this source were not delivered by the observatory until after this paper was submitted; we therefore do not include it in our study.

The data were calibrated as part of the standard reduction procedure by the ALMA support staff (34). These calibrated visibility data sets were then re-examined using both the Common Astronomy Software Application (CASA) package (35) and the Astronomical Image Processing System (AIPS) package (36) to perform additional flagging of sub-standard channels. The visibility sets from the three bands set up for continuum measurements were imaged, using natural weighting, yielding synthesized beams of $1'' \times 0.9''$ (SDSS J081740.52+135134.5) and

1.1'' \times 0.9'' (SDSS J120110.31+211758.5). For SDSS J120110.31+211758.5, we self-calibrated the data set on the quasar continuum emission, resulting in an improvement of $\approx 25\%$ in the root mean square noise of the final image. The visibility data set from the band centered on the redshifted [C II] 158 μ m emission line was imaged, after subtracting any continuum flux, using natural weighting to create a spectral data cube with the same resolution as the continuum image. The spectral cubes were then averaged by four channels to a resolution of 62.5 MHz, corresponding to velocity resolutions of 52 km s⁻¹ and 47 km s⁻¹ for SDSS J081740.52+135134.5 and SDSS J120110.31+211758.5, respectively. After applying the primary beam correction, the final spectral cubes and continuum images were analyzed with the imaging functions provided in CASA. The observed properties of the continuum image and spectral data cube for the two detected galaxies associated with the two DLAs are listed in Table S2.

The optical spectra shown in Fig. 2 were obtained with the High Resolution (HIRES) Spectrograph on the Keck-I telescope (37). The HIRES spectra were obtained on 2011 January 16, 2011 January 24 and 2011 January 25, as part of a program aimed at probing the metallicity evolution of the Universe over cosmic time (6). The total Keck-I integration times were 3 hours (SDSS J081740.52+135134.5) and 2.4 hours (SDSS J120110.31+211758.5), with a full width at half maximum (FWHM) resolution of ~ 8 km s⁻¹. The data were reduced using standard reduction procedures (6). The H I column density was derived from fitting a Voigt profile to the damped Ly α profile. The metallicity of the DLAs ([M/H]) is defined by the ratio of metals to hydrogen compared to the solar abundance (38): $[M/H] = \log N(M) - \log N(H I) - \log N(M)_{\odot} + \log N(H I)_{\odot}$. It was measured from the column density of sulfur and silicon for the DLAs toward SDSS J081740.52+135134.5 and SDSS J120110.31+211758.5, respectively. The properties of the DLAs are listed in Table S3, whereas the properties of the two background quasars are tabulated in Table S4.

Observational Properties

The continuum flux density of each DLA target was determined by integrating the observed flux density over the full extent of the continuum emission feature in the continuum image. The quoted uncertainty is the standard deviation of the observed background noise in the continuum image from an annulus surrounding the detected emission with outer radius three times the size of the observed extent of the emission. The flux density and uncertainty for the velocity bins in the [C II] 158 μ m spectral cube were calculated in a similar manner. From these velocity profiles we determined the FWHM, the redshift and the integrated flux density of the [C II] 158 μ m line, which were converted to the total [C II] 158 μ m line luminosity, $L_{[\text{C II}]}$, using standard procedures (39). We used the fitter function in CASA to determine the physical sizes of both the continuum and the integrated flux density of the [C II] 158 μ m line. These measurements are tabulated in Table S2.

To determine the velocity profile and axis used for creating the p - v diagrams, we generated images of the individual channel maps. These are shown in Figs. S1 and S2. The direction of the axis was determined by fitting a straight line to the positions of maximum flux density in each velocity bin. This yielded position angles of 90 ± 10 degrees east of north and 130 ± 15 degrees west of north for ALMA J081740.86+135138.2 and ALMA J120110.26+211756.2, respectively. Uncertainties were determined through bootstrapping. For ALMA J120110.26+211756.2, the individual channel maps show that at $\sim 65 \text{ km s}^{-1}$, the emission shifts to the northwest by $\sim 0.5''$. This indicates a more complicated velocity profile than a simple rotating disk, such as one arising from a merger or outflow.

In addition to continuum measurements of the galaxies associated with the DLAs, both quasars were also detected in the 400 GHz continuum image. The continuum flux densities for the individual quasars are 0.54 ± 0.08 mJy and 13.15 ± 0.08 mJy, for SDSS J081740.52+135134.5 and SDSS J120110.31+211758.5, respectively. SDSS J120110.31+211758.5 was detected at

high significance, allowing us to search for absorption features in the dust continuum of the quasar from both atoms and molecules. No absorption features were found. The 3σ velocity-integrated line opacity limit for [C II] 158 μm absorption is $\sim 20 \text{ km s}^{-1}$, which corresponds to a C II column density of $N(\text{C II}) < 2.8 \times 10^{18} \text{ cm}^{-2}$ (40). This is in agreement with the estimated column density of C II in the DLA based on the optical observations, $N(\text{C II}) = 1.1 \pm 0.3 \times 10^{17} \text{ cm}^{-2}$. This column density estimate was determined from the Si II column density measurement (6), assuming a solar abundance ratio between carbon and silicon (38).

Physical Parameters of the DLA Host Galaxies

The SFR for the two galaxies is estimated from the continuum luminosity at a rest-frame wavelength of 158 μm , as tabulated in Table S2. To convert these luminosities to SFR estimates, we use the standard calibration obtained from nearby star-forming galaxies (41). Here, we note that our measured luminosities are at a rest wavelength of 158 μm , and not 160 μm , which, for the dust continuum models used in this paper, will overestimate the SFR by less than 5 %. For galaxies with small SFRs, part of the 160 μm emission arises from sources not associated with star formation (42). However, the measured luminosities and predicted SFRs for the two galaxies are large enough that the contribution from non-stellar sources to the 160 μm emission is likely to be negligible. The quoted uncertainties on the SFR are statistical; systematic errors due to the conversion are expected to result in an additional uncertainty by a factor of ~ 2.5 in SFR (41).

The continuum flux density estimate at a rest wavelength of 158 μm can also be used to estimate the total infrared (TIR) luminosity, which is defined as the total luminosity integrated over the interval between 8 μm and 1000 μm . Because we have only a single point for the determination of the far-infrared spectral energy distribution, we apply a range of modified black body models, and fit these models to the measured 158 μm continuum flux density. In

particular, we assume the mid-infrared slope, α , lies in the range $1.5 - 2.5$, the Rayleigh-Jeans index, β , in the range $1.2 - 2.0$, and the dust temperature in the range $25 - 45$ K, consistent with other high redshift studies (24). This results in a systematic uncertainty on the TIR by a factor of 2.5. The quoted uncertainty on the TIR luminosity includes both the uncertainty in the flux density measurement and this systematic uncertainty.

The dynamical mass of the galaxy that gives rise to the [C II] $158\mu\text{m}$ line and the dust continuum emission for ALMA J081740.86+135138.2 can be estimated from the velocity profile of the [C II] $158\mu\text{m}$ line. We estimate the dynamical mass with the equation: $M_{\text{dyn}}/M_{\odot} \approx 1.16 \times 10^5 v_{\text{circ}}^2 D$, where D is the physical diameter (in kpc) of the [C II] $158\mu\text{m}$ emission and v_{circ} is the circular velocity (in km s^{-1}) (43). The circular velocity is estimated by fitting an exponential disk model to the full spectral cube (44). In this exponential disk model, we have fixed the inclination to 90 degrees (i.e., an edge-on disk) since the velocity resolution of the data is insufficient to accurately estimate the inclination. This yields a lower limit to the circular velocity and, hence, a lower limit to the dynamical mass. This lower limit is consistent with the circular velocity estimate obtained using $v_{\text{circ}} = 0.75 \times \text{FWHM}_{[\text{CII}]}$ (43). The resultant dynamical mass estimate is tabulated in Table S2.

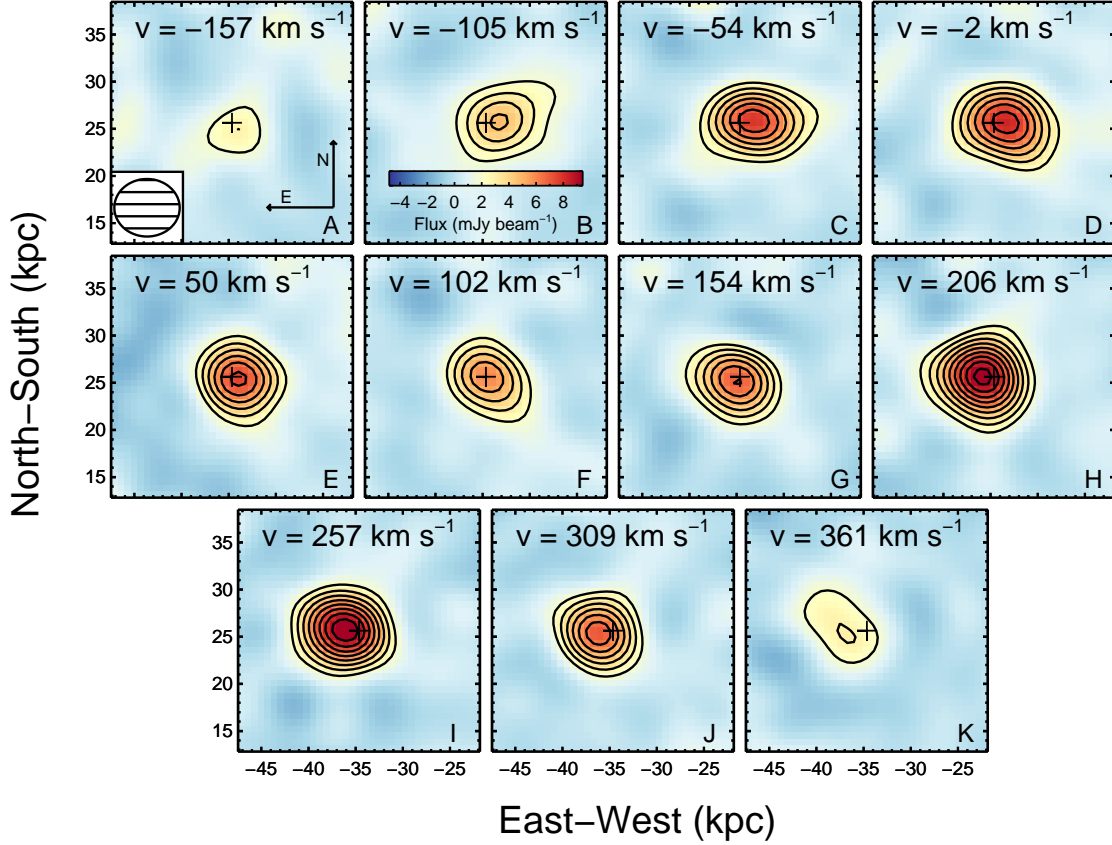


Fig. S1. Channel maps of the [C II] 158 μ m line emission from ALMA J081740.86+135138.2.

The plus symbol indicates the observed central position of the [C II] emission integrated over the full velocity profile (Fig. 1C). Axes give physical distances at the redshift of the DLA, in which the origin is set at the position of the DLA, as in Fig 1. The outer black contour is drawn at 3σ significance with subsequent contours increasing by $\sqrt{2}\sigma$. Velocities are relative to the DLA redshift ($z = 4.2584$). The lower left inset in panel A is the size of the synthesized beam. The flux scale for each panel, given in panel B, is the same for each panel.

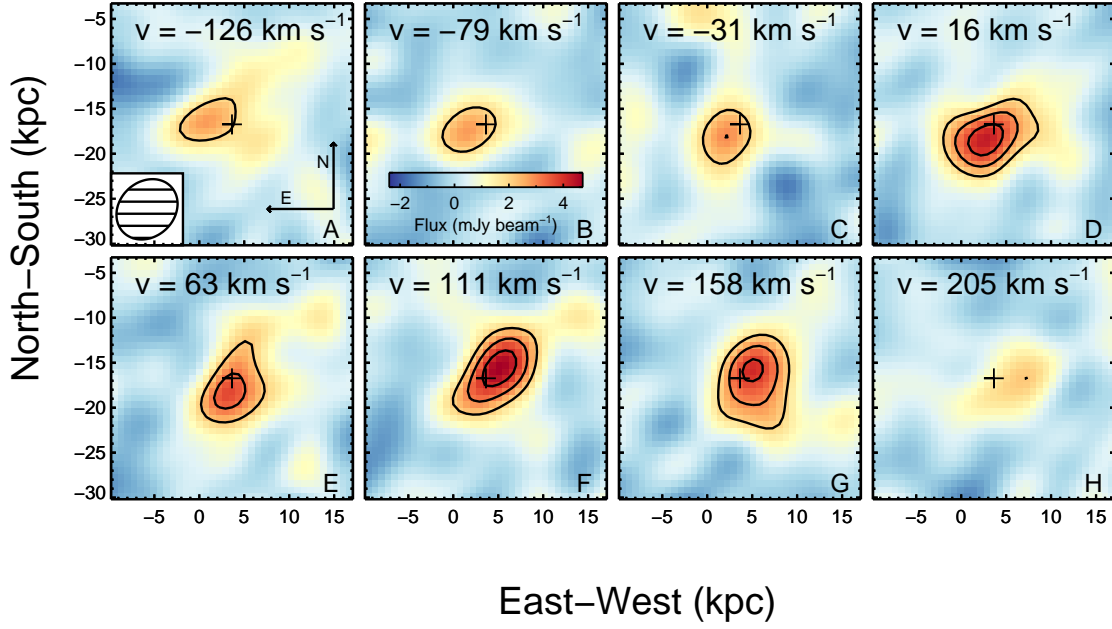


Fig. S2. Channel maps of the [C II] 158 μ m line emission from ALMA J120110.26+211756.2.

The plus symbol indicates the observed central position of the [C II] emission integrated over the full velocity profile (Fig. 1D). Axes give physical distances at the redshift of the DLA, in which the origin is set at the position of the DLA, as in Fig 1. The outer black contour is drawn at 3σ significance with subsequent contours increasing by $\sqrt{2}\sigma$. Velocities are relative to the DLA redshift ($z = 3.7975$). The lower left inset in panel A is the size of the synthesized beam. The flux scale for each panel, given in panel B, is the same for each panel.

Table S1. ALMA Observing Log. Observing log of the ALMA observations for the fields surrounding the quasars SDSS J081740.52+135134.5 and SDSS J120110.31+211758.5. The central frequency (CF), number of channels, and channel width are listed for each of the 4 individual sidebands.

		SDSS J081740.52+135134.5	SDSS J120110.31+211758.5
Date Observed	(UT)	2015 December 30	2015 December 29, 2016 January 1
On-source time	(s)	2782	4596
Right Ascension	(J2000)	08:17:40.53	12:01:10.31
Declination	(J2000)	+13:51:34.6	+21:17:58.5
Number of antennas		39	44
Maximum Baseline	(m)	263	263
Band 1 CF	(GHz)	361.4	396.2
Band 2 CF	(GHz)	363.3	394.5
Band 3 CF	(GHz)	349.3	406.2
Band 4 CF	(GHz)	351.1	407.9
Number of Channels		128	128
Channel width	(MHz)	15.625	15.625

Table S2. Measured properties for the DLA host galaxies. The redshift ($z_{[\text{CII}]}$), peak flux density ($S_{[\text{CII}],\text{peak}}$), velocity integrated flux density ($\int S_{[\text{CII}]}dv$) and full width at half maximum (FWHM $_{[\text{CII}]}$) are measurements from the ALMA spectral data cube, whereas the continuum flux density measurement (S_{cont}) is from the continuum image. The sizes of the continuum emission (A_{cont}) and [C II] emission ($A_{[\text{CII}]}$) are after deconvolution with the ALMA beam.

		ALMA J081740.86+135138.2	ALMA J120110.26+211756.2
Right Ascension	(J2000)	08:17:40.86	12:01:10.26
Declination	(J2000)	+13:51:38.2	+21:17:56.2
$z_{[\text{CII}]}$		4.2601 ± 0.0001	3.7978 ± 0.0001
S_{cont}	(mJy)	1.19 ± 0.11	0.31 ± 0.11
$S_{[\text{CII}],\text{peak}}$	(mJy)	13.1 ± 1.9	7.1 ± 1.7
FWHM $_{[\text{CII}]}$	(km s $^{-1}$)	460 ± 50	330 ± 50
$\int S_{[\text{CII}]}dv$	(Jy km s $^{-1}$)	5.4 ± 0.6	1.9 ± 0.3
A_{cont}	($''$)	$(0.6 \pm 0.2) \times (0.3 \pm 0.3)$	$(< 1.4) \times (< 0.4)^*$
$A_{[\text{CII}]}$	($''$)	$(0.6 \pm 0.2) \times (0.3 \pm 0.2)$	$(1.0 \pm 0.3) \times (0.4 \pm 0.3)$
$\log(L_{\text{TIR}}/L_{\odot})$		$12.0 \pm 0.1 \pm 0.4$	$11.4 \pm 0.2 \pm 0.4$
$\log(L_{[\text{CII}]} / L_{\odot})$		9.48 ± 0.05	8.94 ± 0.07
SFR	($M_{\odot} \text{ yr}^{-1}$)	110 ± 10	24 ± 8
$\log(M_{\text{dyn}}/M_{\odot})$		> 10.8	— †

*Unresolved.

† Not estimated.

Table S3. Measured properties of the DLAs. The DLA redshift (z_{abs}), the neutral hydrogen column density ($N(\text{H I})$) and metallicity ($[\text{M}/\text{H}]$) for the DLAs are derived from the optical absorption spectra (6). The elements used for determining the metallicity are given in parentheses.

		DLA J081740.52+135134.5	DLA J120110.31+211758.5
Right Ascension	(J2000)	08:17:40.52	12:01:10.31
Declination	(J2000)	+13:51:34.5	+21:17:58.4
z_{abs}		4.2584 ± 0.0001	3.7975 ± 0.0001
$\log(N(\text{H I})/\text{cm}^{-2})$		21.30 ± 0.15	21.35 ± 0.15
$[\text{M}/\text{H}]$		-1.15 ± 0.15 (S)	-0.747 ± 0.15 (Si)

Table S4. Measured properties of the Quasars. The position of the quasar, its redshift (z_{QSO}), and photometry (r and i filters) are from the Sloan Digital Sky Survey (SDSS) (45). The quasar continuum flux densities (S_{cont}) at the observed frequency, noted in parentheses, are from the ALMA continuum images.

		SDSS J081740.52+135134.5	SDSS J120110.31+211758.5
Right Ascension	(J2000)	08:17:40.52	12:01:10.31
Declination	(J2000)	+13:51:34.5	+21:17:58.4
z_{QSO}		4.398 ± 0.001	4.579 ± 0.001
r	(AB)	19.22 ± 0.02	20.38 ± 0.03
i	(AB)	19.87 ± 0.02	18.71 ± 0.01
S_{cont}	(mJy)	0.55 ± 0.09 (350GHz)	13.14 ± 0.06 (400GHz)